Investigating the influence of sol-gel bioactive glass 92S6 P123 on 3D-Printed scaffold fabrication

Théodore Berthelot, Ronan Lebullenger, Damien Brézulier, Sylvie Tricot, Sandrine Cammas-Marion, Bertrand Lefeuvre, Anita Lucas

Journal of the Mechanical Behavior of Biomedical Materials 168 (2025) 107041

Contents lists available at ScienceDirect

Journal of the Mechanical Behavior of Biomedical Materials

journal homepage: www.elsevier.com/locate/jmbbm

Investigating the influence of sol-gel bioactive glass 92S6 P123 on 3D-Printed scaffold fabrication

Théodore Berthelot [a,*], Ronan Lebullenger [a], Damien Brézulier [a,b], Sylvie Tricot [a,b], Sandrine Cammas-Marion [c,d], Bertrand Lefeuvre [a], Anita Lucas [a,**]

[a] from Univ Rennes, CNRS, ISCR (Institut des Sciences Chimiques de Rennes) UMR 6226, F-35000, Rennes, France
[b] from Univ Rennes, CHU Rennes, CNRS, ISCR, Pôle Odontologie, UMR 6226, F-35000, Rennes, France
[c] from Univ Rennes, Ecole Nationale Supérieure de Chimie de Rennes, CNRS, ISCR, UMR 6226, ScanMAT, UMS2001, 35000, Rennes, France
[d] from INSERM, INRAE, Univ Rennes, Institut NUMECAN (Nutrition Metabolisms and Cancer) UMR_A 1341, UMR_S 1241, 35000, Rennes, France

A B S T R A C T

Additive manufacturing techniques for scaffold fabrication have shown remarkable potential in tissue engineering and regenerative medicine. In this study, a novel approach involving a composite material consisting of an association of sol-gel bioactive glass, 92S6 P123, with polylactic acid (PLA) was explored to create intricate three-dimensional (3D) scaffolds. The main objective was to analyze the impact of incorporating bioactive glass 92S6 P123 on the properties of 3D-printed scaffolds, subsequently optimizing the architectural design (grid versus gyroid), pore size, and porosity to obtain the best compromise between mechanical properties and porosity. The selected scaffold architecture, the gyroid, exhibits morphological features reminiscent of cancellous bone; this structure was carefully tailored to promote mechanical support and facilitate cell proliferation.

This study sheds light on the significance of incorporating bioactive glass 92S6 P123 into 3D-printed scaffolds. Moreover, the tailored scaffold architecture exhibited promising results in terms of the mechanical stability and cellular invasion. This study contributes to the evolving field of scaffold design for tissue engineering applications, offering insights into the interplay between scaffold composition, architecture, and *in vivo* performance. The knowledge gained from this study holds implications for the development of advanced regenerative therapies and implantable constructs in orthopaedic and tissue engineering disciplines.

1. Introduction

Biomaterials have emerged as crucial components for the advancement of regenerative medicine and tissue engineering applications (Burg et al., 2000). Among these, 3D-printed scaffolds tailored for bone augmentation/replacement have garnered significant attention because of their potential to address critical-sized bone defects and facilitate tissue regeneration (Mohaghegh et al., 2022). The ability to precisely design and manufacture these scaffolds has revolutionized the field, enabling the development of personalized solutions for patients with varying bone deficiencies (Gendviliene et al., 2020).

The integration of bioactive materials within polymeric scaffolds has further expanded their capabilities, aiming to enhance osseointegration and promote osteogenesis (Tavakolizadeh et al., 2017). Notably, bioactive glasses have emerged as promising candidates, possessing the capacity to stimulate cellular responses and facilitate biomaterial-tissue interactions (Jones, 2013).

The concept of employing 3D-printed scaffolds for bone augmentation has progressed remarkably (Nikolova and Chavali, 2019). Traditional approaches for bone defect treatment based on autografts or allografts are often accompanied by limitations, such as donor site morbidity, immune rejection (Franz et al., 2011), and health safety. The use of synthetic scaffolds provides an alternative strategy to circumvent these challenges (Gupta and Meena, 2023).

Early studies focused on using biocompatible and biodegradable polymers as scaffold materials, with porous structures that mimic the cancellous bone matrix to facilitate cell adhesion and proliferation (Bouguéon, 2020; Amini et al., 2012).

The emergence of additive manufacturing technologies, particularly 3D printing (Fiume et al., 2022), has enabled precise fabrication of complex scaffold geometries with controlled porosity, mechanical properties, and architectural designs (Germain et al., 2018). Among the various strategies to improve scaffold performance, the role of architecture is paramount. Scaffold geometry not only influences the mechanical stability of the structure but also regulates critical biological processes such as vascularization, cell migration, and tissue ingrowth. In

* Corresponding author.
** Corresponding author.
E-mail addresses: theodore.berthelot@outlook.fr (T. Berthelot), anita.lucas@univ-rennes.fr (A. Lucas).

https://doi.org/10.1016/j.jmbbm.2025.107041
Received 19 February 2025; Received in revised form 30 April 2025; Accepted 1 May 2025
Available online 2 May 2025

particular, triply periodic minimal surface (TPMS) designs, such as gyroid structures (Khan et al., 2024), have gained attention for their continuous curvature, uniform stress distribution, and resemblance to certain morphological features of cancellous bone (Hameed et al., 2021). Studies have shown that these geometries enhance osteoconduction and load distribution more effectively than traditional strut-based patterns (Berner et al., 2014; Alizadeh-Osgouei et al., 2021). Pore sizes within the 250–500 μm range, often achieved with such designs, are considered optimal for bone tissue ingrowth and angiogenesis (Rustom et al., 2016).

Research efforts have been directed toward optimizing scaffold designs, surface modifications, and material compositions to enhance osteogenesis and overall scaffold performance (Seok et al., 2021). Moreover, the incorporation of bioactive elements, such as bioactive glasses, within these scaffolds improve their performances due to their osteostimulative properties (Kaur et al., 2014). Bioactive glasses (Baino et al., 2018), such as the widely studied 45S5 Bioglass® (Hench, 2006) and other most commonly used like 13–93 (Fu et al., 2008) or S53P4 (Peltola et al., 2006) have demonstrated remarkable potential in promoting bone formation and integration (Chen et al., 2006).

However, these melt derived glasses might be difficult to associate with polymers for the fabrication of 3D scaffolds due to the resulting degradation of the polymer at their contact, particularly the 45S5 Bioglass®.

We developed a sol-gel mesostructured porous bioactive glass 92S6 P123 [25,26] that exhibits high bioactivity and induces selective minerals crystallization at its surface (Aneb et al., 2022), that can easily be associated to polymer for fabrication of 3D composite scaffolds (Owens et al., 2016) because of its low granulometry and its weak impact on polymer's degradation. The designation "92S6" (Letaïef et al., 2014a, 2014b) refers to its nominal molar composition of approximately 92 mol % SiO_2, 6 mol% CaO, and 2 mol% P_2O_5. In terms of weight ratio, this corresponds to 84.82 wt% SiO_2, 10.14 wt% CaO, and 5.04 wt% P_2O_5.

This study investigates the development of 3D-printed scaffolds composed of polylactic acid (PLA) reinforced with a sol-gel bioactive glass (92S6 P123), aiming to provide a structurally robust and biologically favorable implant for bone regeneration. We first assessed the cytocompatibility of the 92S6 P123 glass compared to the clinically established 45S5 Bioglass® (Bretcanu et al., 2009) glass using the acid phosphatase method with Saos-2 osteoblastic and EA.hy926 mesenchymal cell lines. Subsequently, we explored the fabrication of composite PLA (Ilyas et al., 2021)/92S6 P123 filaments suitable for extrusion-based additive manufacturing. These filaments were used to print scaffolds with two distinct architectures: grid and gyroid, to study the effect of geometry on pore size, porosity, and mechanical performance. The gyroid structure was selected for its biomimetic potential and superior interconnected porosity (Hayashi et al., 2023). The effects of the glass on PLA degradation during shaping, as well as the mechanical properties of the resulting scaffolds, were thoroughly analysed.

This study addresses critical aspects of scaffold design, material interactions, and biological responses, contributing to the advancement of 3D-printed biomaterials for bone augmentation and regenerative therapies and contributes to the evolving landscape of bone augmentation biomaterials, focusing on the fabrication of 3D-printed scaffolds incorporating the mesoporous bioactive glass 92S6 P123.

2. Materials and methods

2.1. Chemicals

Tetraethyl orthosilicate (TEOS) (99 % Aldrich, France) was used as our silica source, calcium nitrate tetrahydrate $Ca(NO_3)_2.4H_2O$ (≥99 %, Fluka, Germany) was used as calcium and triethyl phosphate (TEP) (99,8 %, Aldrich, France) was used as our source of phosphorus.

The non-ionic surfactant Pluronic P123 (EO20-PO70-EO20) (Sigma-Aldrich, Germany) was used as our structure directing agent. Water acidified with nitric acid (2 M) was used as solvent.

Polylactide grade PLA RXP 7501 (Resinex, Warszawa, Poland), in powder form, was used as the polymeric matrix for our composite fabrication. According to the manufacturer, this PLA has a density of 1.240 g/cm^3. All materials were used as received without further purification.

2.2. Synthesis of 92S6 P123 using non-ionic surfactant (P123)

The mesoporous 92S6 P123 glass was synthesized by a two-step acid-catalyzed self-assembly process combined with hydrothermal treatment in an organic-inorganic system (Zhao et al., 1998). The P123 (Lei et al., 2013), an amphiphilic block copolymer: poly (ethylene oxide)-block-poly (propylene oxide)- block-poly (ethylene oxide) (PEO-PPO-PEO), was used as organic structure-directing agent. The global synthesis is shown (Fig. 1). Our glass was prepared by dissolving into Teflon beaker, under stirring at 40 °C, 6 g of P123 in 120 ml of 2 M HNO_3 and 30 ml of distilled water solution, until the solution became clear.

Then 3.6 g of TEOS, 0.16 g of TEP and 0.53 g of $Ca(NO_3)_2.4H_2O$ were then added successively at 1-h intervals to the clear solution. The final pH was 0.3. The mixture was stirred at 40 °C for 24 h, and then hydrothermalized at 100 C for 48 h. Without any filtering and washing, the resulting precipitate was directly dried at 100 °C for 24 h in air. The synthesized powders were calcined at 650 °C in air for 6 h to remove the organic structure directing agent completely and converting all chemical species in oxide. The resulting glass (wt% composition: 84.82 % SiO_2 – 10.14 % CaO – 5.04 % P_2O_5) was crushed and sieved to select particule size between 40 and 63 μm. Before use, the resulting powders are stored at room temperature under vacuum to avoid adsorption moisture.

2.3. Cytotoxicity and biological tests

2.3.1. Cell cultures

Two human cell lines were used in this study: endothelial cells EA.hy926 (ATCC, Manassas, VA, USA) and Saos-2 osteoblasts (ATCC, Manassas, VA, USA).

The EA.hy926 and Saos-2 were seeded in Dulbecco's Modified Eagle Medium (Lonza, Belgium) and supplemented with 10 % foetal bovine serum (Gibco, Life Technologies, UK), HEPES 20 mmol/L (Lonza, Belgium), 2 mmol/L glutamine (Biosera, France), and antibiotics (100U/mL penicillin, 100 μg/mL streptomycin; Lonza, Belgium). The cells were cultured in a humidified atmosphere containing 5 % CO_2 at a temperature of 37 °C.

Upon reaching confluence, cells were passaged by trypsin/ethylenediaminetetraacetic acid treatment (EDTA) (Lonza, Belgium).

2.3.2. Preparation of conditioned substrate and cell contact

The evaluated 92S6 P123 glass and the reference bioactive glass 45S5 (Noraker, 45S5 GlassBONE™, France) were in powder form for viability assessment after 24 h or 72 h of culture. The medium was conditioned at 0.2 % or 1 % by weight, DMEM supplemented with penicillin and streptomycin (100U/mL and 100 μg/mL respectively) and HEPES at 20 mmol/L. At the end of incubation, the medium is filtered through 22 μm and supplemented with 10 % foetal calf serum and 1 % glutamine. These glass-to-medium concentrations (0.2 wt% and 1.0 wt %) were selected to reflect both diluted and moderately concentrated extractive conditions, in accordance with standardized *in vitro* protocols for evaluating the cytocompatibility of bioactive glasses.

Suspensions of each cell line in complete medium were prepared and plated at 100μL/well in a 96-well plate. The seeding cell concentration were 5.10^4 cells/mL or 2.10^4 cells/mL, respectively for 24 h (D1) and 72 h (D3) tests. Plates were incubated for 24 h at 37 °C in a humid atmosphere with 5 % CO_2 to allow cell adhesion.

After 24 h, the media were replaced by those conditioned with the different materials.

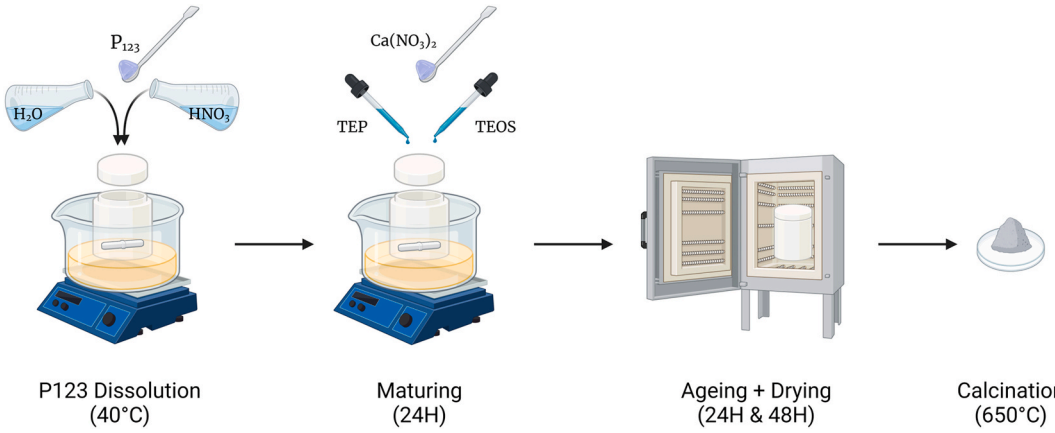

Fig. 1. Synthesis of the 92S6 P123, a bioactive glass synthetized by sol-gel process and its different steps.

2.3.3. Indirect cell proliferation and cytotoxicity test

Cell viability was assessed by the Acid Phosphatase method (Connolly et al., 1986). This test is based on the enzymatic activity of cytoplasmic acid phosphatases that hydrolyse p-nitrophenyl to p-nitrophenol.

The absorbance of p-nitrophenol at 405 nm is proportional to cell numbers within a range of 103–105 cells/mL. After 24 or 72 h of cell culture, quantitative analyses of viable cells were performed by incubation with an ex-expanded 0.1 M acetate - 1 % Triton - 0.1 % 4-nitrophenyl phosphate buffer for 3 h.

At the end of the incubation, 5 µL of NaOH was added to stop the reaction. The optical density was read at a wavelength of 405 nm (Sunrise, Tecan, Männedorf, Switzerland). Cell viability was expressed as a relative value in percentage and compared to 100 % cell viability corresponding to cells in the initial culture media.

2.3.4. Statistical analysis

All experiments were performed in triplicate unless otherwise stated. Results are presented as mean values ± standard deviation (SD). Normality of the data distribution was assessed using the Kolmogorov–Smirnov test (Anonymous, 2008). Given the non-parametric nature of the data, comparisons between groups were conducted using Kruskal–Wallis tests followed by Dunn's post hoc test for multiple comparisons. Statistical significance was set at: (*: $p < 0.05$; **: $p < 0.01$; ***: $p < 0.001$; ****: $p < 0.0001$). All statistical analyses were performed using GraphPad Prism 9 (GraphPad Software, San Diego, CA, USA).

2.4. PLA/92S6 P123 filament fabrication and scaffold preparation

PLA/92S6 P123 composite filament was prepared by mixing 90 wt% of PLA and 10 wt% of 92S6 P123 sol-gel glass powder in planetary mixer (Inversina, Bioengineering, USA) during 6 h. This ratio was selected based on preliminary extrusion trials, which demonstrated that 10 wt% glass ensured sufficient bioactivity while preserving printability and structural integrity of the filament. Higher glass contents (e.g., 15 wt%) led to inhomogeneous extrusion and nozzle clogging. This composite was given the name PL90. The obtained mixture was filamented using an extruder device (Noztech Touch, Noztech, England) at 190 °C. The obtained composite filament had a diameter in the range around 1.50–1.75 mm with a control of the extrusion flow and the winding speed (Fig. 2).

The fused filament fabrication (FFF) method (Ender 3 Pro, Creality, China) (Gao et al., 2021) was used to produce scaffolds while controlling their porosity via filling percentage and geometry (grid versus gyroid). The 3D Scaffolds were modelled first using the software 3D Builder (Anonymous). The 3D file is then converted into a stereolithography file (STL) that can be sent to our slicer software Cura (Anonymous. UltiMaker Cura Easy). Filaments were put in a drying oven 2 h at 50 °C before printing to avoid misprinting due to humidity, which could degrade the filament (Mitchell and Hirt, 2015).

Cuboids with dimensions of 40 mm × 30 mm x 10 mm were designed with gyroid (GYR) and grid (GRI) patterns filling. The scaffolds were given the names GYRx and GRIx for simplicity with the x porosity percentage (x = 50, 60, 70, 80). GYRx and GRIx were printed with PL90 filaments at 190 °C, with a bed temperature at 50 °C and a 0.4 mm

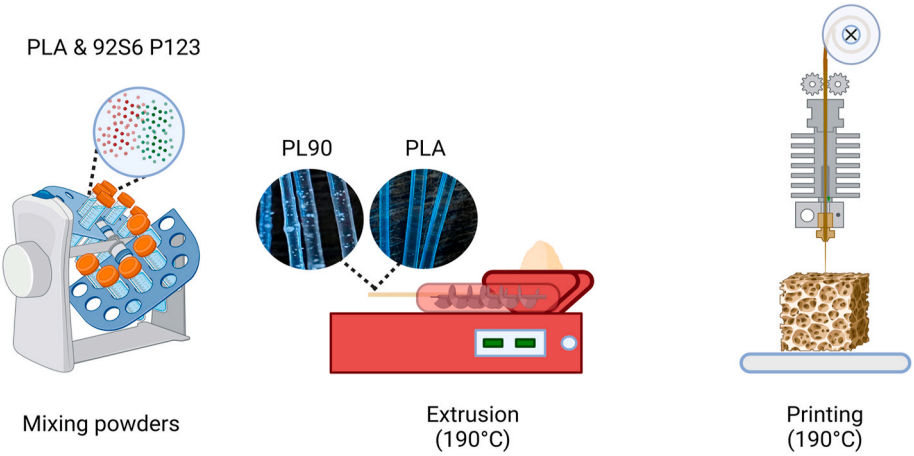

Fig. 2. Fused Filament Fabrication process (FFF) of the PLA filament and the composite PL90 filament to manufacture PLA and composite scaffolds.

nozzle to prevent the accumulation of glass particles during the extrusion of the composite PLA/92S6 P123.

We tried to print composites filaments using a mix between PLA and 45S5 glass (Noraker 45S5 GlassBONE™, France) powder using the same ratio (90/10 wt%) to compare it with our composite filament. A progressive but fast degradation of the PLA was observed making impossible to obtain useable composites filaments.

2.5. Structural, mechanical and physical properties

The possible degradation due to the successive thermal processes of PLA used in our 3D composite scaffolds were analysed using Size Exclusion Chromatography technique (SEC) (Brossard et al., 2021) in tetrahydrofuran (THF) at 40 °C (flow rate = 1.0 mL/min). After dissolution of polymers in THF (2 mg/ml), solutions were injected in a GPC2502 Viscotek apparatus equipped with a refractive index detector Viscotek VE 3580 RI, a guard column Viscotek TGuard, Org 10 × 4.6 mm, a LT5000L gel column (for samples soluble in organic medium) 300 × 7.8 mm and a GPC/SEC OmniSEC Software. All elution curves were calibrated with polystyrene standards. Weight average molar weight (Mw), number average molar mass (Mn) (calculated by dividing the total polymer weight by the total number of polymer molecules) and dispersity (Đ = Mw/Mn) values were measured. Mn can be defined as the statistical average molecular weight of all the polymer chains in the sample. Mw will take in consideration the molecular weight of a chain in determining contributions to the molecular weight average. The more massive the chain, the more the chain contributes to Mw.

For optical imaging, a Keyence VHX-7000 series digital optical microscope was used. It allows 2D and 3D digital modelling of samples with a magnification range of × 100 to ×1000 and a maximum resolution: 4800 × 3600 dpi. Porosity was measured using both optical and electronic imaging. The percentage of porosity was determined using image processing software and compared with the porosity predicted by the Cura slicer software. To observe the topology and the structure of the resulting 3D scaffolds, we used both optical and electronic (SEM) microscopies at room temperature. SEM (JSM-IT300, JEOL ltd, Japan), micrographs were taken at a voltage varying between 15 and 20 kV. Prior to observation, samples were metallized with carbon using a plasma metallizer sputter (Leica ACE600 High Resolution Coater, Leica, USA).

Before mechanical testing, the paved scaffolds were cut into cubes (10 mm × 10 mm x 10 mm) using a circular saw under a stream of water. The mechanical testing of the scaffolds was performed in a compressive mode with a Lloyd 50 K machine (Lloyd Instruments, USA). The controlled displacement speed of the piston was 0.5 mm min^{-1}. Compressive strength values were calculated from the load-displacement curve. The compressive strength test was stopped as soon as one of the scaffold layers broke. Mean values ± SD were calculated for series of 7 tests. The impact of scaffold geometry and porosity was then evaluated.

3. Results and discussion

3.1. Cytotoxicity tests

Relative cell viability obtained after contact of conditioned media for the two glasses, 92S6 P123 and 45S5 GlassBONE™ are presented (Fig. 3). For both cell types, acid phosphatase cytotoxicity assays showed a relative cell survival rate above the 70 % threshold. This result was expressed for concentrations of 0.2 % and 1 %. There was a discrete difference in Saos-2 survival between the 92S6P123 glass-conditioned medium at 24 h and the 45S5 control, for both concentrations ($p < 0.1$). This difference was no longer apparent after 72 h of culture. The same trend was found for EAhy-926 survival at 24 h and 72 h but was not significant. These results are consistent with the absence of cytotoxicity of the sol-gel derived glass 92S6 P123 as for the clinically used for bone regeneration (Philip-et al., 2023; Barrey and Broussolle, 2019) 45S5 GlassBONE™.

This outcome is particularly important because for bioactive glasses, cytotoxicity can occur during *in vitro* culture because of pH increase due to the interaction of bioactive glasses with aqueous media (Ciraldo et al., 2018). The cell survival rate of over 70 % after one or three days of indirect culture attested to the absence of cytotoxicity of glass derived from 92S6 P123 sol-gel. Moreover, no biological difference was demonstrated in comparison with the gold-standard bioactive glass granules 45S5 GlassBONE™, already in clinical use. As a result, the new compound 92S6 P123 appears relevant for use in bone tissue engineering.

3.2. Characterisation of the polymer and composite degradation

The aim is to study the polymer degradation that may occur during the different process phases of polymer and composites scaffolds fabrication through Fused Filament Fabrication (FFF), *i.e.* filaments and scaffolds fabrication. Steric Exclusion Chromatography (SEC) analyses provided an understanding of the degradation profiles of PLA and its composites, with parameters including the number average molar mass (Mn) and the weight average molar mass (Mw). Results of the SEC analyses on initial PLA powder, PLA filament and scaffold, PL90 filament and scaffold are presented below (Fig. 4). It is important to note that the SEC analyses were conducted on single specimens for each material condition. This limitation was due to the restricted quantity of processed samples available for polymer dissolution and filtration.

The transition of PLA from its powder state to filament and scaffold configurations was accompanied by a slight increase in both Mn and Mw. This observation is more likely attributable to sample preparation variability or differences in polymer chain entanglement and crystallinity (Moetazedian et al., 2021), rather than heat-induced polymerization, which is unlikely under the extrusion conditions used here.

Mn and Mw increased significantly post-shaping, which may indicate a molecular rearrangement and a potential cross-linking phenomenon

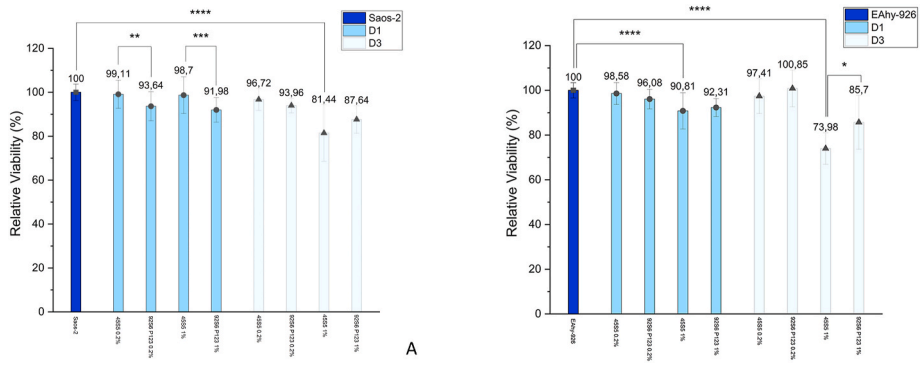

Fig. 3. Acid phosphatase cytotoxicity tests for 45S5 and 92S6 P123 powders. (A) With Osteoblasts Saos-2 (B) With Endothelial cells EA.hy926.

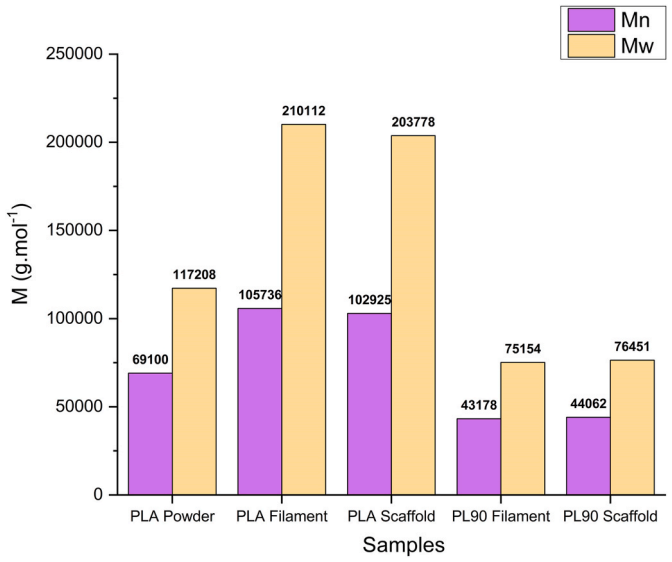

Fig. 4. Number (Mn) and weight (Mw) average molecular weight of PLA as powder, filament, scaffold and the composite PL90 as filament and scaffold.

(Kim and Yoshie, 2018).

Specifically, Mn rose from 69,100 g mol^{-1} (powder) to 105,736 g mol^{-1} (filament), and Mw from 117,208 g mol^{-1} (powder) to 210,112 g mol^{-1} (filament). The PLA scaffold exhibited similar filament values with Mn at 102,295 g mol^{-1} and Mw at 203,778 g mol^{-1}, suggesting a non-impact of shaping conditions. Integration of the sol-gel glass matrix (92S6 P123) into PLA composite formulations resulted in a degradation pattern compared to the PLA itself. The incorporation of the sol-gel glass led to a reduction in both Mn and Mw, indicating a degradation of PLA chains within the composite framework. Mn decreased to 43,178 g mol^{-1} and Mw to 75,154 g mol^{-1} for composite filaments, and to 44,062 g mol^{-1} for Mn and 76,451 g mol^{-1} for Mw in composite scaffolds. The reduction in Mn and Mw observed for the PLA/92S6 P123 composite suggests a modification of the molecular weight distribution due to potential interactions between the glass particles and the polymer matrix during processing. However, these data do not allow for conclusions regarding degradation kinetics, as only static measurements were performed. Comparative experiments with the clinically used glass (45S5) revealed similar degradation behaviours but at a higher level (Chaigneau et al., 2023): the association of PLA and 45S5 did not allow a good filament processing. Indeed, the presence of sodium (Na) ions in 45S5 induced rapid degradation of PLA, manifesting as yellowing and compromised filament clarity (Grémare et al., 2018). This observation of degradation and changing in colour was not observed with the sol-gel glass 92S6 P123. The observed deterioration, attributed to basic catalysis facilitated by sodium ions, underscored the contrasting degradation mechanisms between 45S5 and the sodium free 92S6 P123 sol-gel glass.

Unlike the 45S5-PLA composite, the PL90 filament and scaffold produced did not degrade rapidly. No colour change was observed visually, and the properties of the PLA (viscosity, aspect …) combined with the sol-gel glass were unaffected. Even if the polymer properties are modified by the presence of 92S6P123, stable over time filaments and scaffolds were produced and characterized.

3.3. Structural and mechanical optimization for the 3D-printed scaffolds

The optimization of composite scaffolds is based on the following parameters: porosity pattern (Fig. 5) (gyroid (**A**) or grid (**B**)), porosity percentage x (x = 50,60,70, 80 %) and related pore size and compressive strength.

Through mechanical testing, it was observed that scaffolds with the gyroid pattern consistently exhibited superior mechanical strength (Berner et al., 2014; Mirkhalaf et al., 2021) across all tested porosity levels are shown below (Fig. 6.). The compressive strength of the scaffolds with the gyroid pattern (GYRx) was greater than that of the scaffolds with the grid pattern (GRIx), regardless of the porosity of the scaffold.

At the highest porosity (80 %), compressive strength values of 1.5 ± 0.1 MPa were observed for GRI80, compared with 3.0 ± 0.2 MPa for GYR80. This trend is confirmed as the porosity decreases, with a compressive strength of around 2.2 ± 0.2 MPa for GRI70 compared with 3.8 ± 0.3 MPa for GYR70 at 70 % scaffold porosity.

Finally, at the lowest porosities (60 % & 50 % porosity), the trends observed above were again confirmed but with lower differences. At 60 % porosity, GRI60 had a compressive strength of 8.4 ± 0.9 MPa, compared with 10.4 ± 1.1 MPa for GYR60. At 50 % porosity, these values rose to 15.5 ± 1.4 MPa for GRI50 and 17.2 ± 1.8 MPa for GYR50. The influence of scaffold architecture on mechanical behavior was systematically assessed by comparing grid (GRI) and gyroid (GYR) designs across a range of porosities (50 %–80 %). Our results demonstrate that GYR scaffolds consistently exhibited higher compressive strength than their GRI counterparts at equivalent porosity levels. This difference can

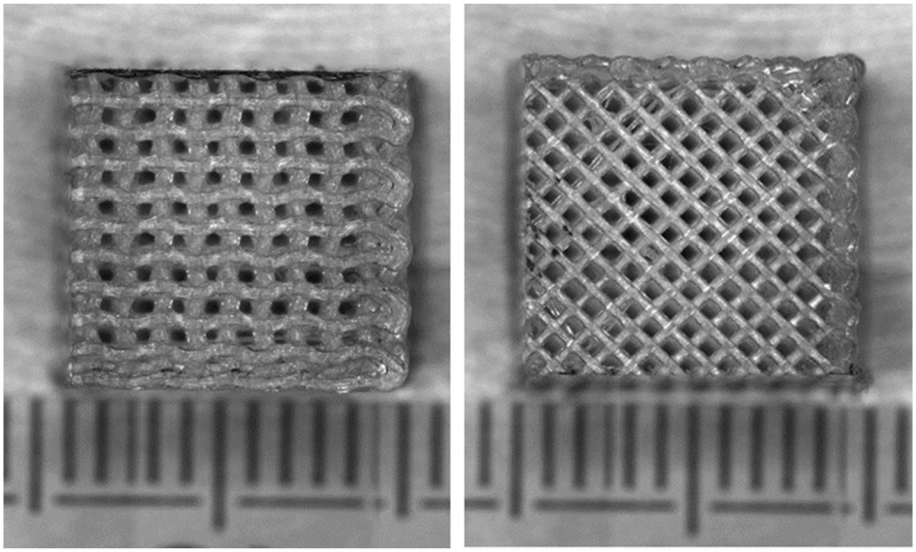

Fig. 5. (A) Gyroid (GYR50) and (B) Grid (GRI50) pattern used for the comparative study (Keyence VHX-7000, X100).

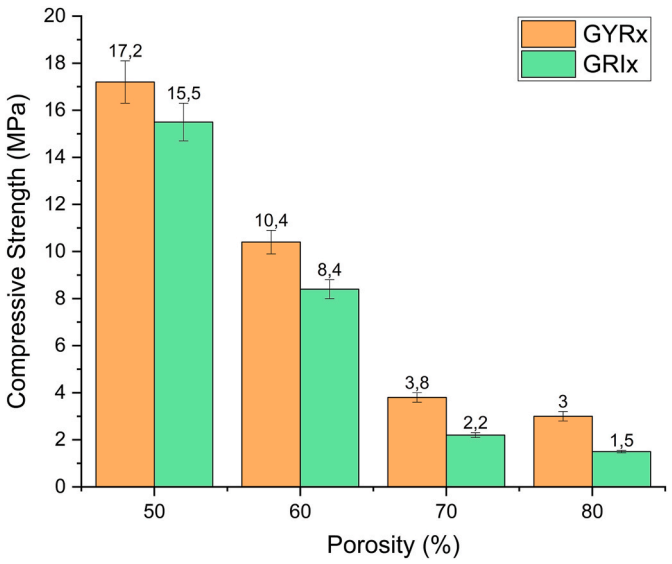

Fig. 6. Mechanical testing using compression comparing the pattern and the porosity of our composite scaffolds.

be attributed to the gyroid's triply periodic minimal surface (TPMS) geometry, which distributes mechanical loads more isotropically and reduces stress concentrations compared to the uniaxial orientation of grid patterns. (Hayashi et al., 2023; Bouyer et al., 2021; Evans, 1969). Moreover, the gyroid structure exhibited a reduced filament usage (~15 % lower than grid at same porosity), confirming its printing efficiency without compromising mechanical stability. This behavior aligns with previous reports showing that TPMS-based designs achieve high strength-to-weight ratios (Berner et al., 2014).

We previously described the observed decrease in compressive strength with the increase of porosity for porous materials (Lucas-et al., 2002). If we apply the Ryshkewitch equation (Ryshkewitch, 1953): $\sigma = \sigma_0 . e^{-c.P}$, with σ as the compressive strength, σ_0 the compressive strength at 0 % porosity, c a constant and P the porosity percentage of our scaffolds. We obtained the following values for our different patterns: $\sigma = 1033.e^{-0.083.P}$ ($R^2 = 0.977$) for the grid pattern (Fig. 7. A) and $\sigma = 389.e^{-0.062.P}$ ($R^2 = 0.979$) for the gyroid pattern (Fig. 7. B).

Using the Ryshkewitch equation revealed that the gyroid architecture better maintained its strength across increasing porosity, exhibiting a lower c constant compared to the grid design. While the grid could theoretically provide superior strength at low porosity, its mechanical performance decreased more sharply with increasing void fraction, making the gyroid a more resilient option for scaffolds targeting moderate porosity ranges. Even if the compressive strength at 0 % porosity σ_0 is higher for the grid pattern compared to the gyroid pattern (see discussion below), the c constant is greater for the grid pattern compared to the gyroid one which means that the compressive strength decreases faster when the porosity is increasing.

From a biological standpoint, GYR scaffolds also exhibited more favorable pore characteristics. For example, at a porosity level of 50 %, the gyroid scaffolds (GYR50) exhibited average interconnected pore size of 313 ± 9 μm, aligning closely with the ideal range for cell colonization and tissue regeneration (250–500 μm) (Rustom et al., 2016). Conversely, grid-patterned scaffolds at the same porosity level (GRI50) displayed a smaller average pore size of 269 ± 8 μm, potentially limiting cellular infiltration and subsequent tissue integration. In addition, and unlike the grid pattern, the gyroid pattern has the advantage of multi-axial connected porosity (x,y,z), giving it increased vascularization and cell invasion compared with the grid pattern whose porosity is uniaxial. The obtained results can be found below (Fig. 8).

The significance of pore size extends beyond mere cell colonization; it directly influences the scaffold's ability to mimic the natural cancellous bone matrix, facilitating nutrient diffusion and waste removal, essential factors for cell survival and proliferation (Abbasi et al., 2020). Furthermore, the gyroid structure exhibits a highly interconnected porosity that is often associated with the architecture of cancellous bone, offering potential advantages in terms of vascularization and tissue ingrowth, which are critical factors for scaffold integration

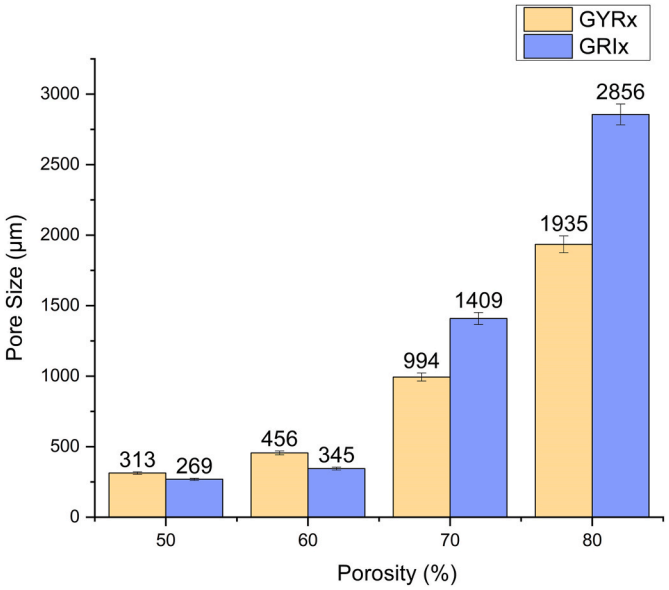

Fig. 8. Pore size of the composite scaffolds regarding their porosity and the pattern used.

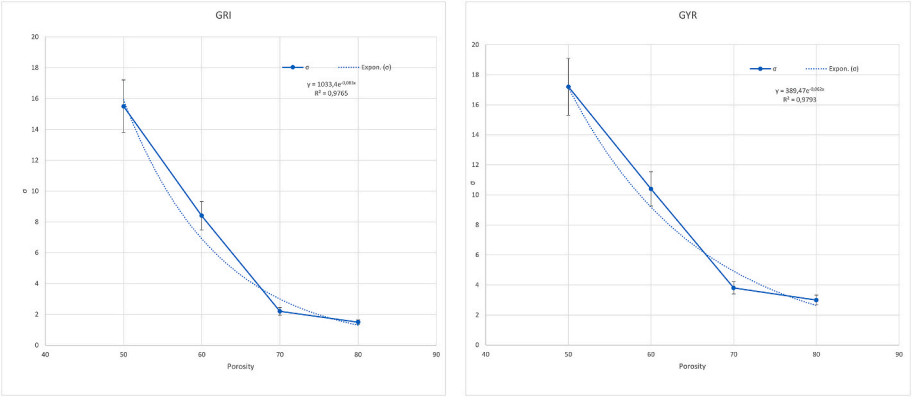

Fig. 7. (A) Compressive strength of gri (GRI) and (B) gyroid (GYR) pattern with different porosities using Ryshkewitch equation (Ciraldo et al., 2018).

(Alizadeh-Osgouei et al., 2021).

The SEM analysis allowed the evaluation of the pore architecture of the scaffolds, revealing that the gyroid pattern facilitated the creation of larger pore sizes compared to the grid pattern. The SEM picture of the GYR50 scaffold and its pores is shown below (Fig. 9). The morphology of the scaffold is a key aspect that affects the migration of cells (Bobbert and Zadpoor, 2017) with an ideal range of 250–500 μm for the pores. We previously highlighted the preferred oriented bone colonization in bone substitute with uniaxial porosity (Lucas et al., 2001). Even if the material is resorbable, a preferred oriented bone ingrowth has restricted bone substitution applications. A 3D colonization of the implant is most often preferable.

Obtained results indicate that the gyroid pattern, particularly at a porosity level of 50 % (GYR50), offers a balance of mechanical robustness, material efficiency, and structural characteristics conducive to bone tissue engineering. The gyroid pattern's superior performance across these critical parameters not only underscores its potential as a preferred scaffold architecture but also highlights the importance of pattern and porosity selection in the design and optimization of scaffolds for biomedical applications (Abbasi et al., 2020). Furthermore, the investigation into material efficiency revealed that gyroid-patterned scaffolds required approximately 15 % less filament than grid-patterned counterparts. That is probably the reason why its σ_0 in the Ryshkewitch equation is lower than the grid pattern. This reduction not only signifies a cost advantage but also contributes to the environmental sustainability of the manufacturing process, a crucial consideration in the development of medical devices.

While the results presented in this study provide compelling evidence for the mechanical and architectural advantages of gyroid-patterned PLA/92S6 P123 scaffolds, several limitations must be acknowledged. First, the mechanical evaluation was limited to uniaxial compression tests. Additional properties such as elastic modulus, toughness, and fatigue resistance remain to be assessed. Furthermore, the degradation behaviour of the PLA matrix was inferred from static SEC measurements and does not represent real-time kinetic degradation. From a modelling perspective, the mechanical behaviour and biological performance could be further optimized using computational simulations such as finite element analysis (FEA) and permeability modelling. These tools would allow for predictive modelling of stress distribution, nutrient diffusion, and cell migration patterns within the scaffold. Finally, while this work focused on cytocompatibility and architecture, *in vivo* studies will be essential to validate the scaffold's regenerative potential and integration with host tissue, which will be presented in a future article.

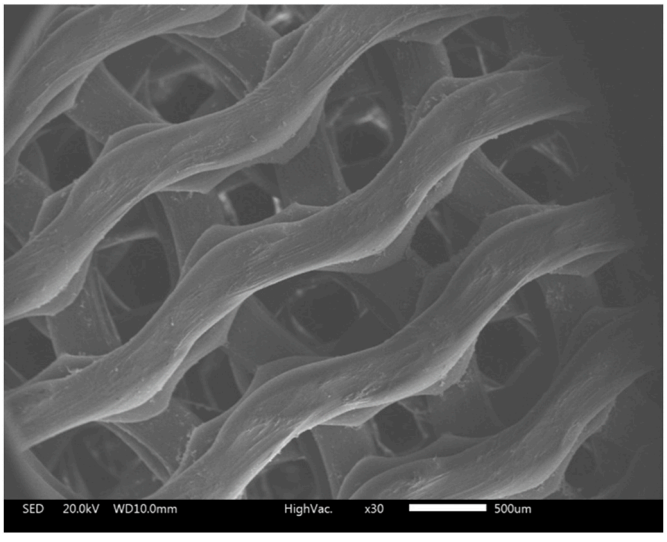

Fig. 9. SEM micrograph of GYR50 composite scaffold (x30).

4. Conclusions

In this study, we investigated the integration of a novel mesoporous bioactive sol-gel glass (92S6 P123) with the biodegradable polymer PLA to fabricate 3D-printed scaffolds tailored for bone regeneration and tissue engineering. The bioactivity and cytocompatibility of 92S6 P123 were first assessed and compared to the clinically used 45S5 Bioglass®. Both materials exhibited non-cytotoxic behavior, maintaining cell viability above the 70 % threshold, thereby validating the potential of 92S6 P123 as a promising candidate for biomedical applications in bone repair.

This glass was then incorporated into a PLA matrix at 10 wt% to produce printable composite filaments compatible with Fused Filament Fabrication (FFF). The processability and thermal behavior of the composite were optimized to preserve polymer integrity and ensure homogenous printing. Size exclusion chromatography (SEC) was used to evaluate the molecular weight evolution of PLA during filament and scaffold formation. The observed variations in Mn and Mw reflected the influence of shaping processes and the presence of glass particles, but did not allow conclusive insights into degradation kinetics.

The mechanical and architectural characterization of the scaffolds highlighted the superior performance of the gyroid pattern over the conventional grid design. Gyroid-based scaffolds, particularly at 50 % porosity, offered an advantageous combination of compressive strength, structural stability, and 3D interconnected porosity, which closely mimics the architecture of trabecular bone. With pore sizes falling within the biologically relevant range (250–500 μm), these structures are expected to enhance cell migration, nutrient diffusion, and ultimately osteointegration.

Among all configurations tested, the GYR50 scaffold emerged as the most promising candidate, combining mechanical robustness, material efficiency, and biomimetic architecture. These attributes suggest a strong potential for its application in non-load bearing or moderately loaded bone defects, particularly in cranio-maxillofacial reconstruction. However, further biological assessments are warranted to evaluate in-vitro osteogenic responses and long-term in-vivo performance.

In summary, this work lays a solid foundation for the development of bioactive, architecturally optimized 3D-printed scaffolds using PLA and sol-gel-derived 92S6 P123 glass. The promising results obtained here call for expanded investigations, including mechanical fatigue testing, advanced computational simulations (e.g., FEA), and in-vivo studies to fully explore the clinical applicability of this composite system. This study also underscores the crucial role of material design and architectural engineering in advancing the field of regenerative medicine.

Funding acquisition

Funding Open access funding provided by Rennes University.

CRediT authorship contribution statement

Théodore Berthelot: Writing – original draft, Validation, Methodology, Investigation, Formal analysis, Data curation, Conceptualization. **Ronan Lebullenger:** Writing – review & editing, Writing – original draft, Validation, Methodology, Conceptualization. **Damien Brézulier:** Writing – review & editing, Validation, Methodology, Investigation, Formal analysis, Data curation. **Sylvie Tricot:** Writing – review & editing, Validation, Methodology, Investigation, Formal analysis, Data curation. **Sandrine Cammas-Marion:** Methodology, Formal analysis, Data curation. **Bertrand Lefeuvre:** Formal analysis, Data curation. **Anita Lucas:** Writing – review & editing, Writing – original draft, Validation, Supervision, Resources, Project administration, Methodology, Conceptualization.

Declaration of competing interest

The authors declare that they have no known competing financial interests or personal relationships that could have appeared to influence the work reported in this paper.

Acknowledgements

Authors would like to acknowledge Dr. Damien Brézulier and Sylvie Tricot for support and help with the cytotoxicity tests. The authors would like to thank Dr. Sandrine Cammas-Marion for support with Steric Exclusion Chromatography analyses. The authors would also like to thank Loïc Joanny and Francis Gouttefangeas and the centre for scanning electron microscopy and microanalysis (CMEBA) of Rennes University for their help and support with SEM analyses.

Data availability

The authors are unable or have chosen not to specify which data has been used.

References

Abbasi, N., Hamlet, S., Love, R.M., et al., 2020. Porous scaffolds for bone regeneration. J. Sci. Adv. Mater. Devices 5 (1), 1–9. https://doi.org/10.1016/j.jsamd.2020.01.007.

Alizadeh-Osgouei, M., Li, Y., Vahid, A., et al., 2021. High strength porous PLA gyroid scaffolds manufactured via fused deposition modeling for tissue-engineering applications. Smart Mater. Med. 2, 15–25. https://doi.org/10.1016/j.smaim.2020.10.003.

Amini, A.R., Laurencin, C.T., Nukavarapu, S.P., 2012. Bone tissue engineering: recent advances and challenges. Crit. Rev. Biomed. Eng. 40 (5), 363–408. https://doi.org/10.1615/critrevbiomedeng.v40.i5.10.

Aneb, K., Oudadesse, H., Khireddine, H., et al., 2022. Study of the effect of ordered porosity and surface silanization on in vitro bioactivity of sol-gel-derived bioactive glasses. Mater. Today Commun. 34, 104992. https://doi.org/10.1016/j.mtcomm.2022.104992.

Anonymous. Create and print 3D objects - windows hardware dev cente. n.d. Available from: https://www.microsoft.com/en-us/3d-print/3d-builder-resources [Last accessed: 10/June/2023].

Anonymous, 2008. Kolmogorov–smirnov test. In: The Concise Encyclopedia of Statistics. Springer, New York, NY, pp. 283–287. https://doi.org/10.1007/978-0-387-32833-1_214.

Anonymous. UltiMaker cura easy-to-use 3D printing software available online. n.d. Available from: https://ultimaker.com/software/ultimaker-cura/[Last accessed: 10/June/2023].

Baino, F., Hamzehlou, S., Kargozar, S., 2018. Bioactive glasses: where are we and where are we going? J. Funct. Biomater. 9 (1), 25. https://doi.org/10.3390/jfb9010025.

Barrey, C., Broussolle, T., 2019. Clinical and radiographic evaluation of bioactive glass in posterior cervical and lumbar spinal fusion. Eur. J. Orthop. Surg. Traumatol. 29 (8), 1623–1629. https://doi.org/10.1007/s00590-019-02477-5.

Berner, A., Woodruff, M.A., Lam, C.X.F., et al., 2014. Effects of scaffold architecture on cranial bone healing. Int. J. Oral Maxillofac. Surg. 43 (4), 506–513. https://doi.org/10.1016/j.ijom.2013.05.008.

Bobbert, F.S.L., Zadpoor, A.A., 2017. Effects of bone substitute architecture and surface properties on cell response, angiogenesis, and structure of new bone. J. Mater. Chem. B 5 (31), 6175–6192. https://doi.org/10.1039/C7TB00741H.

Bouguéon, G., 2020. Formulation de nanosystèmes biocompatibles pour l'ingénierie tissulaire par impression 3D (bioprinting). Phdthesis. Université de Bordeaux.

Bouyer, M., Garot, C., Machillot, P., et al., 2021. 3D-printed scaffold combined to 2D osteoinductive coatings to repair a critical-size mandibular bone defect. Mater. Today Bio 11, 100113. https://doi.org/10.1016/j.mtbio.2021.100113.

Bretcanu, O., Chatzistavrou, X., Paraskevopoulos, K., et al., 2009. Sintering and crystallisation of 45S5 bioglass® powder. J. Eur. Ceram. Soc. 29 (16), 3299–3306. https://doi.org/10.1016/j.jeurceramsoc.2009.06.035.

Brossard, C., Vlach, M., Vène, E., et al., 2021. Synthesis of Poly(Malic acid) derivatives end-functionalized with peptides and preparation of biocompatible nanoparticles to target hepatoma cells. Nanomaterials 11 (4), 958. https://doi.org/10.3390/nano11040958.

Burg, K.J.L., Porter, S., Kellam, J.F., 2000. Biomaterial developments for bone tissue engineering. Biomaterials 21 (23), 2347–2359. https://doi.org/10.1016/S0142-9612(00)00102-2.

Chaigneau, L., Perrot, A., Brezulier, D., et al., 2023. Bioresorbable polylactic acid (PLA) and bioactive glasses (BG) composite: influence of gold coated of BG powder on mechanical properties and chemical reactivity. J. Mech. Behav. Biomed. Mater. 138, 105571. https://doi.org/10.1016/j.jmbbm.2022.105571.

Chen, Q.Z., Thompson, I.D., Boccaccini, A.R., 2006. 45S5 bioglass®-derived glass–ceramic scaffolds for bone tissue engineering. Biomaterials 27 (11), 2414–2425. https://doi.org/10.1016/j.biomaterials.2005.11.025.

Ciraldo, F.E., Boccardi, E., Melli, V., et al., 2018. Tackling bioactive glass excessive in vitro bioreactivity: preconditioning approaches for cell culture tests. Acta Biomater. 75, 3–10. https://doi.org/10.1016/j.actbio.2018.05.019.

Connolly, D.T., Knight, M.B., Harakas, N.K., et al., 1986. Determination of the number of endothelial cells in culture using an acid phosphatase assay. Anal. Biochem. 152 (1), 136–140. https://doi.org/10.1016/0003-2697(86)90131-4.

Evans, F.G., 1969. The mechanical properties of bone. Artif. Limbs 13 (1), 37–48.

Fiume, E., Massera, J., D'Ambrosio, D., et al., 2022. Robocasting of multicomponent sol-gel–derived silicate bioactive glass scaffolds for bone tissue engineering. Ceram. Int. 48 (23, Part A), 35209–35216. https://doi.org/10.1016/j.ceramint.2022.08.121.

Franz, S., Rammelt, S., Scharnweber, D., et al., 2011. Immune responses to implants - a review of the implications for the design of immunomodulatory biomaterials. Biomaterials 32 (28), 6692–6709. https://doi.org/10.1016/j.biomaterials.2011.05.078.

Fu, Q., Rahaman, M.N., Sonny, Bal B., et al., 2008. Mechanical and in vitro performance of 13–93 bioactive glass scaffolds prepared by a polymer foam replication technique. Acta Biomater. 4 (6), 1854–1864. https://doi.org/10.1016/j.actbio.2008.04.019.

Gao, X., Qi, S., Kuang, X., et al., 2021. Fused filament fabrication of polymer materials: a review of interlayer bond. Addit. Manuf. 37, 101658. https://doi.org/10.1016/j.addma.2020.101658.

Gendviliene, I., Simoliunas, E., Rekstyte, S., et al., 2020. Assessment of the morphology and dimensional accuracy of 3D printed PLA and PLA/hAp scaffolds. J. Mech. Behav. Biomed. Mater. 104, 103616. https://doi.org/10.1016/j.jmbbm.2020.103616.

Germain, L., Fuentes, C.A., van Vuure, A.W., et al., 2018. 3D-printed biodegradable gyroid scaffolds for tissue engineering applications. Mater. Des. 151, 113–122. https://doi.org/10.1016/j.matdes.2018.04.037.

Grémare, A., Guduric, V., Bareille, R., et al., 2018. Characterization of printed PLA scaffolds for bone tissue engineering. J. Biomed. Mater. Res. 106 (4), 887–894. https://doi.org/10.1002/jbm.a.36289.

Gupta, K., Meena, K., 2023. Artificial bone scaffolds and bone joints by additive manufacturing: a review. Bioprinting 31, e00268. https://doi.org/10.1016/j.bprint.2023.e00268.

Hameed, P., Liu, C.-F., Ummethala, R., et al., 2021. Biomorphic porous Ti6Al4V gyroid scaffolds for bone implant applications fabricated by selective laser melting. Prog. Addit. Manuf. 6 (3), 455–469. https://doi.org/10.1007/s40964-021-00210-5.

Hayashi, K., Kishida, R., Tsuchiya, A., et al., 2023. Superiority of triply periodic minimal surface gyroid structure to strut-based grid structure in both strength and bone regeneration. ACS Appl. Mater. Interfaces 15 (29), 34570–34577. https://doi.org/10.1021/acsami.3c06263.

Hench, L.L., 2006. The story of bioglass®. J. Mater. Sci. Mater. Med. 17 (11), 967–978. https://doi.org/10.1007/s10856-006-0432-z.

Ilyas, R.A., Sapuan, S.M., Harussani, M.M., et al., 2021. Polylactic acid (PLA) biocomposite: processing, additive manufacturing and advanced applications. Polymers 13 (8), 1326. https://doi.org/10.3390/polym13081326.

Jones, J.R., 2013. Review of bioactive glass: from hench to hybrids. Acta Biomater. 9 (1), 4457–4486. https://doi.org/10.1016/j.actbio.2012.08.023.

Kaur, G., Pandey, O.P., Singh, K., et al., 2014. A review of bioactive glasses: their structure, properties, fabrication and apatite formation. J. Biomed. Mater. Res. 102 (1), 254–274. https://doi.org/10.1002/jbm.a.34690.

Khan, P.A., Raheem, A., Kalirajan, C., et al., 2024. In vivo assessment of a triple periodic minimal surface based biomimmetic gyroid as an implant material in a rabbit tibia model. ACS Mater. Au 4 (5), 479–488. https://doi.org/10.1021/acsmaterialsau.4c00016.

Kim, C., Yoshie, N., 2018. Polymers healed autonomously and with the assistance of ubiquitous stimuli: how can we combine mechanical strength and a healing ability in polymers? Polym. J. 50 (10), 919–929. https://doi.org/10.1038/s41428-018-0079-x.

Lei, C., Chen, B., Li, X., et al., 2013. Non-destructively shattered mesoporous silica for protein drug delivery. Microporous Mesoporous Mater. 175, 157–160. https://doi.org/10.1016/j.micromeso.2013.03.022.

Letaïef, N., Lucas-Girot, A., Oudadesse, H., et al., 2014a. Effect of aging temperature on the structure, pore morphology and bioactivity of new sol–gel synthesized bioglass. J. Non-Cryst. Solids 402, 194–199. https://doi.org/10.1016/j.jnoncrysol.2014.06.005.

Letaïef, N., Lucas-Girot, A., Oudadesse, H., et al., 2014b. Investigation of the surfactant type effect on characteristics and bioactivity of new mesoporous bioactive glass in the ternary system SiO2–CaO–P2O5: structural, textural and reactivity studies. Microporous Mesoporous Mater. 195, 102–111. https://doi.org/10.1016/j.micromeso.2014.03.035.

Lucas, A., Gaudé, J., Carel, C., et al., 2001. A synthetic aragonite-based ceramic as a bone graft substitute and substrate for antibiotics. Int. J. Inorg. Mater. 3 (1), 87–94. https://doi.org/10.1016/S1466-6049(00)00058-1.

Lucas-Girot, A., Langlois, P., Sangleboeuf, J.C., et al., 2002. A synthetic aragonite-based bioceramic: influence of process parameters on porosity and compressive strength. Biomaterials 23 (2), 503–510. https://doi.org/10.1016/S0142-9612(01)00132-6.

Mirkhalaf, M., Wang, X., Entezari, A., et al., 2021. Redefining architectural effects in 3D printed scaffolds through rational design for optimal bone tissue regeneration. Appl. Mater. Today 25, 101168. https://doi.org/10.1016/j.apmt.2021.101168.

Mitchell, M.K., Hirt, D.E., 2015. Degradation of PLA fibers at elevated temperature and humidity. Polym. Eng. Sci. 55 (7), 1652–1660. https://doi.org/10.1002/pen.24003.

Moetazedian, A., Gleadall, A., Han, X., et al., 2021. Mechanical performance of 3D printed polylactide during degradation. Addit. Manuf. 38, 101764. https://doi.org/10.1016/j.addma.2020.101764.

Mohaghegh, S., Hosseini, S.F., Rad, M.R., et al., 2022. 3D printed composite scaffolds in bone tissue engineering: a systematic review. Curr. Stem Cell Res. Ther. 17 (7), 648–709. https://doi.org/10.2174/1574888x16666210810111754.

Nikolova, M.P., Chavali, M.S., 2019. Recent advances in biomaterials for 3D scaffolds: a review. Bioact. Mater. 4, 271–292. https://doi.org/10.1016/j.bioactmat.2019.10.005.

Owens, G.J., Singh, R.K., Foroutan, F., et al., 2016. Sol–gel based materials for biomedical applications. Prog. Mater. Sci. 77, 1–79. https://doi.org/10.1016/j.pmatsci.2015.12.001.

Peltola, M., Aitasalo, K., Suonpää, J., et al., 2006. Bioactive glass S53P4 in frontal sinus obliteration: a long-term clinical experience. Head Neck 28 (9), 834–841. https://doi.org/10.1002/hed.20436.

Philip-Alliez, C., Fievet, L., Serratrice, N., et al., 2023. Cone Beam-CT-Based bone volume assessments of alveolar synthetic bone graft GlassBONE^{TM} in cleft lip and palate patients: a retrospective study. J. Maxillofac. Oral Surg. https://doi.org/10.1007/s12663-023-02056-6.

Rustom, L.E., Boudou, T., Lou, S., et al., 2016. Micropore-induced capillarity enhances bone distribution in vivo in biphasic calcium phosphate scaffolds. Acta Biomater. 44, 144–154. https://doi.org/10.1016/j.actbio.2016.08.025.

Ryshkewitch, E., 1953. Compression strength of porous sintered alumina and zirconia. J. Am. Ceram. Soc. 36 (2), 65–68. https://doi.org/10.1111/j.1151-2916.1953.tb12837.x.

Seok, J.M., Choe, G., Lee, S.J., et al., 2021. Enhanced three-dimensional printing scaffold for osteogenesis using a mussel-inspired graphene oxide coating. Mater. Des. 209, 109941. https://doi.org/10.1016/j.matdes.2021.109941.

Tavakolizadeh, A., Ahmadian, M., Fathi, M.H., et al., 2017. Investigation of osteoinductive effects of different compositions of bioactive glass nanoparticles for bone tissue engineering. ASAIO J. 63 (4), 512–517. https://doi.org/10.1097/MAT.0000000000000509.

Zhao, D., Feng, J., Huo, Q., et al., 1998. Triblock copolymer syntheses of mesoporous silica with periodic 50 to 300 angstrom pores. Science 279 (5350), 548–552. https://doi.org/10.1126/science.279.5350.548.